OPEN ACCESS

University of BRISTOL

University of Bristol - Explore Bristol Research
General rights

Fe-FeO and Fe-Fe₃C melting relations at Earth's Core-Mantle Boundary conditions: implications for a volatile-rich or oxygen-rich core

G. Morard[1*], D. Andrault[2], D. Antonangeli[1], Y. Nakajima[3,4], A.L. Auzende[1,5], E. Boulard[6], S. Cervera[1], A. Clark[1], O.T. Lord[7], J. Siebert[8], V. Svitlyk[9], G. Garbarino[9], M. Mezouar[9]

[1]*Institut de Minéralogie, de Physique des Matériaux, et de Cosmochimie (IMPMC), Sorbonne Universités - UPMC, UMR CNRS 7590, Muséum National d'Histoire Naturelle, IRD UMR 206, F-75005 Paris, France.*

[2]*Laboratoire Magmas et Volcans, CNRS-OPGC-IRD, Université Blaise Pascal, Clermont-Ferrand, France*

[3]*Materials Dynamics Laboratory, RIKEN SPring-8 Center, RIKEN, Hyogo 679-5148, Japan*

[4]*Department of Physics, Kumamoto University, Kumamoto 860-8555, Japan*

[5]*Univ. Grenoble Alpes, Univ. Savoie Mont Blanc, CNRS, IRD, IFSTTAR, ISTerre, F-38000 Grenoble, France*

[6]*Synchrotron Soleil, L'Orme des Merisiers, Saint Aubin, France*

[7]*School of Earth Sciences, University of Bristol, Wills Memorial Building, Queen's Road, Bristol, BS8 1RJ, UK*

[8]*Institut de Physique du Globe de Paris, Université Paris 7, F-75005 Paris, France*

[9]*European Synchrotron Radiation Facility, Grenoble, France*

[*] e-mail: guillaume.morard@impmc.upmc.fr

Abstract

Eutectic melting temperatures in the Fe-FeO and Fe-Fe₃C systems have been determined up to 150 GPa. Melting criteria include observation of a diffuse scattering signal by *in situ* X-Ray diffraction, and textural characterisation of recovered samples. In addition, compositions of eutectic liquids have been established by combining *in situ* Rietveld analyses with *ex situ* chemical analyses. Gathering these new results together with previous reports on Fe-S and Fe-Si systems allow us to discuss the specific effect of each light element (Si, S, O, C) on the melting properties of the outer core. Crystallization temperatures of Si-rich core compositional models are too high to be compatible with the absence of extensive mantle melting at the core-mantle boundary (CMB) and significant amounts of volatile elements such as S and/or C (>5 at%, corresponding to >2 wt%), or a large amount of O (>15 at% corresponding to ~5 wt%) are required to reduce the crystallisation temperature of the core material below that of a peridotitic lower mantle.

1. Introduction

The Earth's core is composed of iron and nickel alloyed with lighter elements such as O, Si, S, C or H (Poirier, 1994). The chemical composition of the core was set during its segregation at the base of a primitive magma ocean. Recent models of core-mantle differentiation, based on experimental determinations of the partitioning of siderophile elements between silicate melts and liquid metals, indicate that Si and O are potential major light element candidates (R. a. Fischer et al., 2015; J Siebert et al., 2013). The amount of volatile light elements, such as S, C or H, incorporated into the Earth's core would be limited, based on the Earth's elemental volatility trend relative to chondritic material (Dreibus and Palme, 1995; McDonough, 2003). In these studies the abundance of volatile elements is below 5 at% in the core, and compositions with Si and/or O greater than 10 at% are favoured. Yet, the actual

49   abundance of volatile elements in the core could be significantly higher than these estimations

50   if the Earth has accreted from differentiated volatile-bearing bodies (Chabot, 2004) and/or if

51   non-equilibrium processes have dominated core segregation (Rudge et al., 2010).

52   Each light element uniquely affects the physical and chemical properties of metallic iron

53   (e.g. density, bulk modulus, liquid/solid chemical partitioning) (Morard et al., 2014). It is well

54   known that at ambient pressure, light elements alloyed to iron show a range of topologies in

55   their phase diagrams including quasi-perfect solid solutions (like Fe-Si), eutectic behaviour

56   (like Fe-C and Fe-S) or liquid-liquid immiscibility gaps (like Fe-O). These differences can help

57   to discriminate which elements are present in the Earth's core through comparison of laboratory

58   measurements with seismological observations. The determination of melting curves for Fe-

59   alloys at core pressures is crucial to assess the core temperature at the inner core boundary

60   (ICB) where the liquid Fe-alloy crystallizes, and hence, the temperature profile throughout the

61   entire core. In particular, assessing the composition and temperature of the eutectic point in

62   these iron alloys systems would allow us to constrain the degree to which each light element

63   depresses the melting point of pure iron and hence the crystallisation temperature of the core

64   alloy at the ICB.

65   The temperature at the core-mantle boundary (CMB; 330 GPa) is related to that at the

66   ICB (136 GPa), and is significantly higher than the crystallisation temperature of the core alloy.

67   This is because the geotherm matches the melting temperature only at the ICB, whereas it

68   follows an adiabat throughout the outer core with the maximum difference between the two

69   curves occurring at the CMB. The determination of the crystallization temperature of Fe-alloys

70   at 136 GPa thus provides a lower bound to the CMB temperature that has to be corrected

71   upwards by several hundreds of kelvin.

72   Seismological features potentially related to mantle melting at the base of the mantle, the

73   so-called ultra-low velocity zones (ULVZ) (Williams and Garnero, 1996), are not global, and

are located in well-defined geographic regions. The solidus temperature of peridotitic mantle is found to be around 4200 K (Andrault et al., 2011; Fiquet et al., 2010). Further, the fact that basaltic crust subducted to the CMB is not thought to be systematically partially molten based on seismological studies (Garnero et al., 2016; McNamara et al., 2010), potentially provides a lower bound for the CMB temperature at the basalt solidus of 3750-4000K (Andrault et al., 2014; Pradhan et al., 2015).

In the present study we determine both the temperature and composition of the eutectic in the Fe-FeO and Fe-Fe$_3$C systems at CMB pressures. Combining our new results with previously determined phase diagrams in the Fe-FeSi and Fe-Fe$_3$S systems, the temperature of each Fe-X alloy is compared with the melting temperature of mantle materials to determine the viability of the presence of Si, O, C, and S in the core. In view of the non-ubiquitous melting of silicates at the CMB (Garnero et al., 2016), this leads us to conclude that the core must either contain >5at% volatile elements (S, C) or >15at% O.

2. Methods

2.1 Starting materials

For the Fe-FeO system, a first batch of samples (Fe-10 wt.% O) consisted of a mixture of powders of Fe (99.99 %; Alfa Aesar) and FeO (99.95 %; Alfa Aesar), finely ground together in an agate mortar. A second batch of samples was synthesized by sputtering iron onto a glass slide under O$_2$ flow (DEPHIS Company). The chemical composition of this alloy was measured by an electron microprobe as 5.3 ± 0.8 wt.% O. For the Fe-C system, homogeneous samples were prepared by induction melting in a water-cooled Cu crucible under a He atmosphere, at the ICMPE laboratory in Thiais, France. First, ribbon specimens were produced by the planar flow casting technique. These alloys were then re-melted and ejected through a pressurized quartz nozzle on a rotating cooled Cu-base wheel under 1 bar He atmosphere. The chemical

4

99   composition of 1.5 wt. % C was determined by a Cameca SX100 electron microprobe at

100   Camparis, Université Pierre et Marie Curie, using a cold catcher to minimize carbon

101   contamination during the analysis. Operating conditions were 15 kV and 40 nA for a counting

102   time of 20 s on peak and 10 s on background. The standard for carbon was stoichiometric Fe3C

103   and pure Fe used as a blank between each measurement. We used a defocused beam of ~20 μm

104   to average the compositions of quenched melts.

105

106   **2.2 *In situ* XRD experiment**

107   *In situ* angle dispersive X-ray diffraction (XRD) experiments were performed at

108   beamline ID27 of the European Synchrotron Radiation Facility (ESRF) in Grenoble, France

109   (Mezouar et al., 2005).

110   Pressure was generated with Le Toullec-type laser-heated diamond anvil cells (LH-

111   DACs) containing diamond anvils with either 250 μm flat culets, or culets of 150 μm, 100 μm

112   or 70 μm beveled to 300 μm diameter depending upon target pressure. Diamonds with conical

113   supports (Boehler and De Hantsetters, 2004) were used in order to collect diffracted X-rays out

114   to a 2-theta angle of 70 degrees. A flake of metal sample was sandwiched between two dry KCl

115   layers, which were loaded in a hole drilled in a pre-indented rhenium gasket. The size and

116   thicknesses of the different parts depends on the culet size of the anvil. KCl acts as the thermal

117   insulator and as a soft pressure medium at high temperature, ensuring relatively good

118   hydrostatic conditions, with the further advantage of being chemically inert towards iron alloys

119   (no reaction between KCl and Fe liquid alloys has been noted from either XRD or chemical

120   analysis of our samples). The pressure medium also helps to trap the liquid metal, thus enabling

121   the collection of a strong diffuse scattering signal.

122

123   Samples were heated on both sides by two continuous wave Nd:YAG fiber lasers (TEM

124   00) providing a maximum total power of 200 W. Laser spots were more than 20 µm in diameter

125   at the sample. Temperatures were obtained via the spectroradiometric method, using reflective

126   collecting optics (Schultz et al., 2005). Temperature was measured on both sides at the center

127   of the hot spot region by analyzing the thermal emission from a 2*2 µm area selected by a

128   pinhole placed at the entrance of the spectrometer. Incoming laser power was independently

129   tuned on the two sample sides in order to minimize axial temperature gradients.

130   Typical exposure times for diffuse scattering measurements were between 5 and 10

131   seconds. Temperature uncertainties are essentially related to radial and axial temperature

132   gradients. Considering the >20 µm diameter laser spot and the 4 µm diameter X-ray beam used

133   in this study, the uncertainty in the radial direction is less than 50 K (Schultz et al. 2005). The

134   double-sided laser heating and the controlled geometry of the assembly maintain the uncertainty

135   in the axial direction below 100 K. We therefore apply a temperature uncertainty of ±150 K for

136   our experiments (Morard et al. 2011).

137   Pressure was determined using the thermal equation of state of KCl (Dewaele et al.,

138   2012). Following (Campbell et al., 2009), the temperature of the KCl is assumed to be the

139   average between the temperature of the diamond culet at 300K and the temperature measured

140   at the sample surface (in view of the high thermal conductivity of diamond, the entire anvil is

141   assumed to be at room temperature). Pressure uncertainties are estimated from the width of the

142   KCl diffraction peaks (±1 GPa) and the uncertainty in the temperature measurement. For

143   experiments performed off-line, pressure at ambient temperature was measured using the

144   Raman signal of the diamond culet (Akahama and Kawamura, 2004), and an empirical law is

145   used to estimate the thermal pressure (Andrault et al., 1998).

146

2.3 Analysis of recovered samples and off-line experiments

Samples were systematically recovered after high-pressure high-temperature experiments, and cross sections of laser-heated hotspots were prepared by focused ion beam (FIB) milling. The off-line experiments employed Al_2O_3 as both the pressure transmitting medium and thermal insulation. Typical textures observed in cross sections are in good agreement with the sequence of X-ray diffraction patterns recorded during laser heating (Figure 1).

The experimental protocol implemented here for the analysis of recovered samples combined femtosecond pulsed laser machining, ion polishing and FIB cutting. First, the sample and a portion of the surrounding gasket were cut using a femtosecond pulsed laser and placed on a thin glass slide (Figure S1A). Several samples could be positioned on the same glass slide, with their heated spots at the edge of the glass slide. All parts sticking out of the glass slide are then removed using ion polishing (Figure S1B). Then, the entire glass slide is coated with carbon to make it conductive. Final cutting is performed using the FIB (Figure S1C). This method allows us to perform chemical analysis without removing the laser-heated hotspot from its surroundings. The sample holder could be turned at 90° to perform conventional energy dispersive (EDS) or wavelength dispersive (WDS) analysis.

Analysis of oxygen in an Fe-bearing sample using a scanning electron microscope (SEM) or electron probe in either EDS or WDS mode is difficult due to interferences between the emission lines of oxygen and iron. Quantification of oxygen contents below approximately 2wt.% is practically impossible. Validity of measurements below this limit is not guaranteed, therefore this limit corresponds to a lower bound for our experimental results (Table 1). Accordingly, we have not been able to estimate if there is an increase in O content in the eutectic liquid in the pressure range between 20 and 50 GPa, compared to multi-anvil experiments reporting ~1wt%O at 20 GPa (Tsuno and Ohtani, 2009).

172   Chemical analysis exhibits a significant Al signature in the melt recovered from

173   experiments performed using Al_2O_3 as the pressure medium. At the temperatures of our

174   experiments, however, previous work reports no Al solubility in liquid iron alloys (Badro et al.

175   2016). The Al signal could therefore come from the surrounding pressure medium. We then

176   removed the hypothetical Al_2O_3 contribution from the chemical analysis of the quenched

177   metallic melt (i.e. all the Al plus sufficient O to maintain the Al_2O_3 stoichiometry), obtaining

178   chemical compositions of liquid metal in the experiments performed with Al_2O_3 as the pressure

179   medium that are in excellent agreement with those performed in KCl at similar pressures (Table

180   1).

181

2.4 Rietveld analysis of XRD patterns from quenched liquid

183   Knowledge of the composition of the studied liquid is required in order to process its

184   diffuse scattering signal. Turning off the laser quenches the liquid into a metallic glass alloy as

185   indicated by the persistence of the diffuse signal. This glass can be recrystallized to produce

186   well-defined diffraction rings when the sample is re-heated to around ~1400 K for a few minutes

187   (Figure 2). Such powder diffraction patterns can be processed by the Rietveld method (using

188   the GSAS software), in order to refine the phase proportions (Fe, Fe_3C, FeO, etc.) in the

189   recrystallized assemblage. In this way, we derived the melt composition before quenching, by

190   assuming that the amount of carbon and oxygen in solid Fe under the moderate temperatures of

191   re-heating is negligeable (Fei and Brosh, 2014; O. T. Lord et al., 2009; H Ozawa et al., 2008)

192   (Table 2).

193

2.5 Validity of diffuse scattering as a melting criterion

195   The appearance of diffuse scattering as a criterion for the onset of melting has been

196   widely used in recent years (Andrault et al., 2006; Fischer et al., 2013; Morard et al., 2011).

While the validity of this XRD melting diagnostic has been recently disputed on the base of a XANES study on pure iron, which proposed a significantly lower melting curve (Anzellini et al. 2013; Aquilanti et al. 2015;), subsequent measurements suggested other causes for the discrepancy than the different x-ray diagnostics, including chemical reactions or other metrological issues (Torchio et al., 2016).

Irrespective of this, when using XRD to investigate the melting of a eutectic system it is worth keeping in mind that the volume of liquid, which translates into the intensity of the diffuse scattering signal, will depend on the initial sample composition, and specifically on how much this differs from the eutectic composition at a given pressure. The accuracy of the melting temperature determination could therefore be affected if the intensity of the diffuse signal is too weak (i.e. for a liquid fraction below the detection limit). In other words, upon temperature increase, the first melt produced has the eutectic composition and, in equilibrium melting processes, the melt fraction is controlled by the starting composition. As a direct consequence of this, the farther from the eutectic composition the starting material is, the smaller the melt volume produced at the solidus temperature will be. Raising temperature further increases the melt volume making it more easily detectable. Accordingly, the intrinsic detection limit of a given technique might bias solidus temperature determination, leading to an overestimation of the true thermodynamic value. We have assessed this effect in the Fe-S system, which is experimentally easier to study, by measuring the melting temperature for different starting compositions. At a pressure of 62 GPa, for which the eutectic composition is~10 wt% S (Mori et al., 2016), eutectic temperatures of 2150±150 K, and between 2150 and 2270 K, were respectively measured for sample compositions of 12wt%S (Seiji Kamada et al., 2012; Morard et al., 2008) and 6wt%S (Figure S2). Such an agreement shows that even for compositional variations of several wt %, the produced volume of melt is sufficient to yield a measureable diffuse signal at the solidus temperature.

222   In order to further confirm that the diffuse signal arises from the presence of melt, the

223   texture of recovered samples has been investigated by SEM and compared to the *in situ* XRD

224   experiment (see Figure 1 for an example for the Fe-FeO system). Before the appearance of

225   diffuse scattering in the XRD patterns, the texture shows interconnected FeO and Fe grains

226   typical of subsolidus conditions (LH2 on Figure 1). When the diffuse scattering is observed, it

227   correlates with the formation of a melt pool in the laser hotspot (LH1 on Figure 1). At the onset

228   of melting, migration of some chemical elements can contribute to the formation of a melt pool

229   with a significant size, irrespective of the sample composition.

230

231   **3. Results**

232   **3.1 Eutectic melting temperature of Fe-O and Fe-C alloys**

233   We first consider the melting behaviour of Fe-O (5 and 10 wt.% O) and Fe-C (1.5 wt.%

234   C) alloys obtained by *in situ* XRD in the LH-DAC up to ~150 GPa (Figure 3; Table S1, S2 and

235   S3). We stress that the onset of melting was detected at the same temperatures (within

236   experimental uncertainties) for the two different Fe-FeO compositions, as expected for a

237   eutectic system. For the Fe-1.5 wt.% C sample, diffraction patterns suggest that Fe_3C is the

238   solid phase coexisting with the liquid over the entire investigated pressure range. This is in

239   agreement with previous thermodynamic models (Fei and Brosh, 2014), as well as with a

240   previous LH-DAC study at core pressures (Tateno et al., 2010), but it contrasts with another

241   LH-DAC study suggesting that the liquidus phase would change to Fe_7C_3 at around 120 GPa

242   on the basis of an extrapolation of lower pressure data (O T Lord et al., 2009).

243   For both systems the eutectic melting curves are in very good agreement with those

244   established at more moderate pressures using other diagnostics, such as temperature vs. laser

245   power relations in the Fe-C system (O T Lord et al., 2009), the disappearance of diffraction

246   lines in the Fe-FeO system (Seagle et al., 2008), as well as recent diffuse scattering

247 measurements (Liu et al., 2015). For both Fe-O and Fe-C systems, all experimental data points

248 fall within 200 K of the Simon-Glatzel fits performed up to 150 GPa (Table 3). The Fe-Fe$_3$C

249 eutectic temperature is systematically lower than that of Fe-FeO (Figure 3). At the CMB

250 pressure of 136 GPa, eutectic temperatures in the Fe-FeO and Fe-Fe$_3$C systems are 3200 K and

251 2900 K, respectively.

252

253 **3.2 Eutectic composition of Fe-O and Fe-C alloys**

254 The light element content of the eutectic liquid is another parameter of major importance.

255 To determine this, two different techniques have been used in the present study. First, after FIB

256 cutting, quenched-liquid pools of several microns in diameter were revealed and chemically

257 analyzed (Figure 1). In a complementary approach, the Rietveld analysis of XRD patterns from

258 quenched samples gives results in excellent agreement with the chemical analysis. It should be

259 noted that significant carbon contamination of Fe-O liquids could occur as a result of the alloy

260 reacting with the diamonds as emphasized by the presence of Fe$_3$C in the diffraction patterns.

261 This carbon contamination happens after melting, as a result of melt migrating through the

262 pressure medium and coming into contact with the diamond as indicated by the absence of Fe$_3$C

263 diffraction peaks before melting. The carbon contamination appears to remain low when the

264 oxygen content in the eutectic liquid rises above 80 GPa (Figure 4). This drastic increase in O

265 content in the Fe-alloy could be associated with the metallization of the B1 structure of the FeO

266 end-member (Ohta et al., 2012), potentially enhancing the compatibility between FeO and Fe

267 liquids. We note that our chemical analyses below 80 GPa are significantly different from

268 previous LH-DAC experiments (Seagle et al. 2008) and thermodynamic calculations

269 (Komabayashi, 2014) which both suggest a drastic increase in O content in the Fe-alloy below

270 50 GPa. On the other hand, all data sets agree above 80 GPa. Thus, we can safely estimate the

271 eutectic composition in the Fe-FeO system at the CMB pressure of 136 GPa to be ~11 wt.%

272 oxygen (~30 at.% O) (Figure 4).

273   Only Rietveld analysis is available for the Fe-C system (Figure 2). Despite large error

274 bars, we find that the C content of the eutectic liquid falls in the range of previous determination

275 using the large volume apparatus (Fei and Brosh, 2014), in contrast with another report using

276 the LH-DAC (O. T. Lord et al., 2009) (Figure 5). We note, however, that based on our

277 diffraction patterns we identify the presence of Fe_3C, in coexistence with Fe before the eutectic

278 melting, up to 150 GPa. This is not the structure expected from thermodynamic calculations

279 (Fei and Brosh, 2014) or lower pressure experiments (O. T. Lord et al., 2009). From our study

280 and previous thermodynamic calculations (Fei and Brosh, 2014), we estimate the eutectic

281 composition at the CMB (136 GPa) is 2.6 ± 1 wt.% C (11 ± 4 at.% C) at 136 GPa (Figure 5).

282

283 **4. Discussion**

284 **4.1 Melting temperature depression in binary Fe-alloys at the CMB pressure**

285   In order to model the melting behaviour of binary alloys at the CMB pressure, a reference

286 melting temperature should is required for pure Fe. Unfortunately, the melting curve of pure Fe

287 is still subject to controversy. Recent XRD measurements made in the LH-DAC, in good

288 agreement with shock-wave experiments and ab initio calculations, yield a melting temperature

289 for iron at CMB pressure of 4200 K (Anzellini et al., 2013). Conversely, a more recent study

290 using X-ray absorption spectroscopy suggested a much lower melting temperature (Aquilanti

291 et al., 2015) in good agreement with the eutectic melting curve we have measured for the Fe-

292 Fe_3C system. It is therefore plausible that the XANES experiments (Aquilanti et al., 2015) was

293 affected by carbon contamination, which is hardly detectable and quantifiable in the absence of

294 XRD measurements or chemical analysis of recovered samples, neither of which were

performed in the XANES study. Therefore, we consider the XRD study by Anzellini et al. (2013) to be a more reliable reference for the melting of pure Fe.

Supporting our assertion of a high melting point for pure iron, the melting curve of the Fe-18at%Si alloy obtained by XRD diagnostics (Fischer et al., 2013) and further confirmed by thermal signal processing (Lord et al., 2014) is very close to that of pure iron obtained using XRD diagnostics (Figure 6). In the Fe-Si system, recent melting experiments at CMB conditions indicate a eutectic composition of 3wt%Si (Ozawa et al., 2016). The melting temperature increases for compositions on the Si-rich side relative to the eutectic point, and this could explain the close or even higher melting point of Fe-18 at.% Si, leading to a melting temperature of 4300 K (Lord et al., 2014) (Figure 6). It appears therefore that Si has essentially no effect on the melting temperature of iron in the range of compositions from 0-15at%Si. In contrast, lower melting points have been reported for higher Si contents, up to more than 16 wt%Si (27.5 at%Si) (Asanuma et al., 2010; Morard et al., 2011), suggesting a peritectic behavior. In all cases, such large Si contents are not directly relevant to the Earth's core.

In the Fe-S system, the eutectic composition has been widely reported, and recent studies at core pressures suggest a eutectic sulfur content at CMB pressure of 15 (±5) at%S, for a melting temperature of 2870 (±200) K (S Kamada et al., 2012; Morard et al., 2011). Both the eutectic temperature and the composition in the Fe-S system appear similar to those in the Fe-C system.

In the present study, we used the Simon–Glatzel equation to model the melting curves for all the iron alloys, the refined parameters of which are summarized in Table 3. We used a single relation to fit all melting curves over the entire pressure range, as we did not find any evidence for significant inflexions that could arise from an intersection of a solid-solid phase boundary with the melting curve (Figure 6). For the following discussion we also assume to be linear the liquidus line linking the melting point of pure iron at the CMB (4200 K at 136 GPa (Anzellini

320 et al., 2013) and the eutectic melting point for each binary system (Table 4). Combining

321 measurements presented here with data from the literature, we obtain liquidus lines on the iron-

322 rich side of the key binary diagrams (Fe-O, Fe-Si, Fe-S and Fe-C) at the pressure of the CMB

323 (136 GPa) (Figure 7A). Volatile elements (C and S) induce the strongest melting point

324 depression. The effect of hydrogen cannot be addressed properly due to the lack of melting data

325 in the Fe-H system at the pressure of the CMB, though it has been speculated that its effect is

326 even larger than C or S (Sakamaki et al., 2009). The effect of O is smaller, but still much more

327 significant than the effect of Si.

328

4.2 Implications for the composition of the outer core

330 Recent core formation models based on metal/silicate partitioning under high pressure

331 suggest that Si and/or O could be the main light elements in the Earth's core in view of the

332 expected loss of volatile elements (C, S and H) during the early differentiation of the Earth (R.

333 a. Fischer et al., 2015; J Siebert et al., 2013). These models propose either high Si (8.5 wt%Si

334 or 15.5 at% Si) (R. a. Fischer et al., 2015) and/or high O (up to 5wt% O or 15.5 at%O) (J Siebert

335 et al., 2013) contents, depending on the average oxidation state of the material that accreted to

336 form the Earth. Most likely, the Earth's core contains a mixture of light elements, which can

337 chemically interact with each other. In the Fe-Si-O system, recent observations suggest a

338 temperature-dependent liquid immiscibility with exsolution of SiO_2 across a large part of the

339 ternary diagram, leading to an incompatibility between Si and O in the Earth's core (Hirose et

340 al., 2017). Therefore, knowledge of the binary Fe-Si and Fe-O melting diagrams seems

341 sufficient to describe behaviours of Si- and/or O-rich core models. In this study, we also assume

342 that the melting point depression caused by the volatile elements C and S, remains linear with

343 respect to the addition of these elements into an Fe-alloy, irrespectively of the content in other

344   light elements, including O and/or Si. For low solute content, this approximation fulfils physical

345   properties such as density or compressibility (Badro et al., 2014).

346   This parameterization of the melting temperature depression associated with the presence

347   of light elements can be used to place new constraints on the composition of the outer core. The

348   crystallization temperature of core material pins the geotherm at 330 GPa, the pressure at the

349   inner–outer core boundary (ICB). Across the liquid outer core (extending from 135 to 330 GPa),

350   the geotherm is expected to follow an adiabat with a P-T slope that is less steep than the melting

351   curve (otherwise the outer core would not be liquid). At the CMB, the core temperature is

352   therefore significantly higher, by a temperature difference ΔT_{CMB}, than the crystallization

353   temperature of the outer-core alloy. The quantitative evaluation of ΔT_{CMB} requires

354   reconstructing both the melting and the adiabatic temperature profiles, across the range of core

355   pressures. This calculation implies large extrapolations due to the limited pressure range

356   covered by the relevant experiments (up to ~150 GPa). Nonetheless, ΔT_{CMB} has been estimated

357   in previous studies at 400K (Anzellini et al., 2013) or at 900K (Komabayashi, 2014). As such,

358   we can take as reference for the temperature at the CMB the melting temperature of the core-

359   forming alloy at 136 GPa plus an additional 400-900 K (Figure 7B).

360   An upper bound for the current CMB temperature is ~4150 K, which corresponds to the

361   mantle melting (solidus) temperature at 136 GPa (Andrault et al., 2011; Fiquet et al., 2010).

362   Accordingly, as shown in Figure 7B, there are Fe-alloy compositions that are too refractory to

363   be compatible with the absence of ubiquitous melt at the base of the mantle and the

364   crystallization of the inner core at 330 GPa (<5at% C or S or <15at.% O). Significant amounts

365   of C, S or O in the Fe-alloy are required to lower the outer core crystallization temperature

366   enough that the temperature at the CMB is not at or above the peridotite solidus, which in turn

367   undermine the validity of all compositional models with high Si content (e.g. 15 at% as

368   suggested by Fischer et al, 2015). In addition, Si strongly affects the liquid density and

369 compressibility (Badro et al., 2014; Morard et al., 2013), as well as the sound velocity of solid

370 alloys (Antonangeli et al., 2010), to the point that Si-rich alloys do not agree with PREM values.

371 Furthermore, a core composition with Si content on the Si-rich side of the eutectic point would

372 crystallize a CsCl (B2)-type solid phase that is insufficiently dense (Ozawa et al., 2016). In

373 contrast, compositional models with high oxygen contents (O>10-15 at%) are compatible with

374 the absence of widespread mantle melting at the CMB. The actual abundance of oxygen in the

375 Earth's core is still debated on the basis of geochemical arguments and core differentiation

376 models (R. A. Fischer et al., 2015; Julien Siebert et al., 2013), but the physical properties of Fe-

377 O liquid alloys seem to match seismological observations (Badro et al. 2014). We stress also

378 that oxygen is favoured in order to explain the density jump at the ICB, as it is the only light

379 element that partitions sufficiently strongly into the liquid phase (Alfè et al., 2002; Ozawa et

380 al., 2008). Inclusion of ~ 5at% C or S into the outer core would also favour an efficient lowering

381 of the Fe-alloy crystallization temperature (Figure 7B). The substitution of O by C or S in the

382 outer-core reduces the crystallization temperature by ~100 and ~50 K/at.%, respectively, and

383 this effect is even more pronounced if volatiles elements replace Si instead of O.

384

385 **5. Conclusion**

386   Melting curves up to the pressure of the CMB for two different iron-alloy systems (Fe-

387 O and Fe-C) were obtained by *in-situ* XRD. The major XRD criterion used for the determination

388 of eutectic melting temperatures, i.e. the occurrence of a diffuse scattering signal from the

389 liquid, has been confirmed by textural analysis of recovered samples. We constrained the

390 composition of the eutectic melt *in situ* from the Rietveld analysis of the crystallised liquid,

391 supplemented with ex-situ analysis of recovered samples using electron micro-beam

392 techniques.

393   These results have been combined with previous studies on the Fe-S and Fe-Si systems

394   in order to assess the role of each light element (S, Si, O and C) on the melting temperature

395   depression of each binary Fe-alloy compared to pure Fe. We then compare the melting

396   temperature of various compositional models for the Earth's core and the temperature at the

397   CMB. Recent Si-rich core compositional models based on metal-silicate partitioning

398   experiments (e.g. Fischer et al. 2015) would lead to a CMB temperature that would produce

399   ubiquitous melting at the bottom of the silicate mantle, in striking contradiction with the seismic

400   observations. The presence of a significant amount of volatile elements (S and C) in the Earth's

401   core appears to be the only alternative to a very O-rich core.

402

References

Akahama, Y., Kawamura, H., 2004. High-pressure Raman spectroscopy of diamond anvils to 250 GPa: Method for pressure determination in the multimegabar pressure range. J. Appl. Phys. 96, 3748–3751. doi:10.1063/1.1778482

Alfè, D., Gillan, M.J., Price, G.D., 2002. Composition and temperature of the Earth's core constrained by combining ab initio calculations and seismic data. Earth Planet. Sc. Lett. 195, 91–98.

Andrault, D., Bolfan-Casanova, N., Lo Nigro, G., Bouhifd, M.A., Garbarino, G., Mezouar, M., 2011. Solidus and liquidus profiles of chondritic mantle: Implication for melting of the Earth across its history. Earth Planet. Sc. Lett. 304, 251–259.

Andrault, D., Fiquet, G., Itié, J.P., Richet, P., Gillet, P., Häusermann, D., Hanfland, H., 1998. Thermal pressure in the laser heated diamond anvil cell : An X-ray diffraction study. Eur. J. Miner. 10, 931–940.

Andrault, D., Morard, G., Bolfan-Casanova, N., Ohtaka, O., Fukui, H., Arima, H., Guignot, N., Funakoshi, K., Lazor, P., Mezouar, M., 2006. Study of partial melting at high pressure using in situ X-ray diffraction. High Press. Res. 26, 267–276. doi:10.1080/08957950600897013

Andrault, D., Pesce, G., Bouhifd, M.A., Bolfan-Casanova, N., Hénot, J.-M., Mezouar, M., 2014. Melting of subducted basalt at the core-mantle boundary. Science 344, 892–5. doi:10.1126/science.1250466

Antonangeli, D., Siebert, J., Badro, J., Farber, D.L., Fiquet, G., Morard, G., Ryerson, F.J., 2010. Composition of the Earth's inner core from high-pressure sound velocity measurements in Fe-Ni-Si alloys. Earth Planet. Sc. Lett. 295, 292–296.

Anzellini, S., Dewaele, A., Mezouar, M., Loubeyre, P., Morard, G., 2013. Melting of iron at Earth's inner core boundary based on fast X-ray diffraction. Science (80-.). 340, 464–6. doi:10.1126/science.1233514

Aquilanti, G., Trapananti, A., Karandikar, A., Kantor, I., Marini, C., Mathon, O., Pascarelli, S., Boehler, R., 2015. Melting of iron determined by X-ray absorption spectroscopy to 100 GPa. Proc. Natl. Acad. Sci. 112, 12042–12045. doi:10.1073/pnas.1502363112

Asanuma, H., Ohtani, E., Sakai, T., Terasaki, H., Kamada, S., Kondo, T., Kikegawa, T., 2010. Melting of iron–silicon alloy up to the core–mantle boundary pressure: implications to the thermal structure of the Earth's core. Phys. Chem. Miner. 37, 353–359.

Badro, J., Côté, A.S., Brodholt, J.P., 2014. A seismologically consistent compositional model of Earth's core. Proc. Natl. Acad. Sci. U. S. A. 111, 7542–5. doi:10.1073/pnas.1316708111

Badro, J., Siebert, J., Nimmo, F., 2016. An early geodynamo driven by exsolution of mantle components from Earth's core. Nature 536, 326–328. doi:10.1038/nature18594

Boehler, R., 1993. Temperatures in the Earth's core from melting-point measurements of iron at high static pressures. Nature 363, 534–536. doi:10.1038/363534a0

Campbell, A.J., Danielson, L., Righter, K., Seagle, C.T., Wang, Y., Prakapenka, V.B., 2009. High pressure effects on the iron-iron oxide and nickel-nickel oxide oxygen fugacity buffers. Earth Planet. Sci. Lett. 286, 556–564. doi:10.1016/j.epsl.2009.07.022

445   Chabot, N.L., 2004. Sulfur contents of the parental metallic cores of magmatic iron
446   meteorites. Geochim. Cosmochim. Acta 68, 3607–3618.

447   Dewaele, A., Belonoshko, A.B., Garbarino, G., Occelli, F., Bouvier, P., Hanfland, M.,
448   Mezouar, M., 2012. High-pressure-high-temperature equation of state of KCl and KBr.
449   Phys. Rev. B - Condens. Matter Mater. Phys. 85, 1–7. doi:10.1103/PhysRevB.85.214105

450   Dreibus, G., Palme, H., 1995. Cosmochemical constraints on the sulfur content in the Earth's
451   core. Geochim. Cosmochim. Acta 60, 1125–1130.

452   Fei, Y., Brosh, E., 2014. Experimental study and thermodynamic calculations of phase
453   relations in the Fe-C system at high pressure. Earth Planet. Sci. Lett. 408, 155–162.
454   doi:10.1016/j.epsl.2014.09.044

455   Fiquet, G., Auzende, A.L., Siebert, J., Corgne, A., Bureau, H., Ozawa, H., Garbarino, G.,
456   2010. Melting of peridotite at 140 Gigapascals. Science (80-.). 329, 1516–1518.

457   Fischer, R.A., Campbell, A.J., Reaman, D.M., Miller, N.A., Heinz, D.L., Dera, P.,
458   Prakapenka, V.B., 2013. Phase relations in the Fe–FeSi system at high pressures and
459   temperatures. Earth Planet. Sc. Lett. 373, 54–64.

460   Fischer, R.A., Nakajima, Y., Campbell, A.J., Frost, D.J., Harries, D., Langenhorst, F.,
461   Miyajima, N., Pollok, K., Rubie, D.C., 2015. High pressure metal-silicate partitioning of
462   Ni, Co, V, Cr, Si, and O. Geochim. Cosmochim. Acta 167, 177–194.
463   doi:10.1016/j.gca.2015.06.026

464   Fischer, R. a., Nakajima, Y., Campbell, A.J., Frost, D.J., Harries, D., Langenhorst, F.,
465   Miyajima, N., Pollok, K., Rubie, D.C., 2015. High pressure metal–silicate partitioning of
466   Ni, Co, V, Cr, Si, and O. Geochim. Cosmochim. Acta 167, 177–194.
467   doi:10.1016/j.gca.2015.06.026

468   Garnero, E.J., McNamara, A.K., Shim, S.-H., 2016. Continent-sized anomalous zones with
469   low seismic velocity at the base of Earth's mantle. Nat. Geosci. 9, 481.
470   doi:10.1038/ngeo2733

471   Hirose, K., Morard, G., Sinmyo, R., Umemoto, K., Hernlund, J., Helffrich, G., Labrosse, S.,
472   2017. SiO2 crystallization and compositional evolution of the Earth's core. Nature In
473   press.

474   Huang, H., Fei, Y., Cai, L., Jing, F., Hu, X., Xie, H., Zhang, L., Gong, Z., 2011. Evidence for
475   an oxygen-depleted liquid outer core of the Earth. Nature 479, 513–517.

476   Kamada, S., Ohtani, E., Terasaki, H., Sakai, T., Miyahara, M., Ohishi, Y., Hirao, N., 2012.
477   Melting relationships in the Fe-Fe3S system up to the outer core conditions. Earth Planet.
478   Sci. Lett. 359–360, 26–33. doi:10.1016/j.epsl.2012.09.038

479   Kamada, S., Ohtani, E., Terasaki, H., Sakai, T., Miyahara, M., Ohishi, Y., Hirao, N., 2012.
480   Melting relationships in the Fe–Fe3S system up to the outer core conditions. Earth
481   Planet. Sc. Lett. 359–360, 26–33.

482   Komabayashi, T., 2014. Thermodynamics of melting relations in the system Fe-FeO at high
483   pressure: Implications for oxygen in the Earth's core. J. Geophys. Res. Solid Earth 119,
484   4164–4177. doi:10.1002/2014JB010980.Received

485   Liu, J., Li, L., Hrubiak, R., Smith, J.S., 2015. Origins of ultra-low velocity zones through
486   mantle-derived metallic melt. Pnas 1–28. doi:10.1073/pnas.1519540113

487   Lord, O.T., Walter, M.J., Dasgupta, R., Walker, D., Clark, S.M., 2009. Melting in the Fe-C

488 system to 70 GPa. Earth Planet. Sci. Lett. 284, 157–167. doi:10.1016/j.epsl.2009.04.017

489 Lord, O.T., Walter, M.J., Dasgupta, R., Walker, D., Clark, S.M., 2009. Melting in the Fe-C
490 system to 70 GPa. Earth Planet. Sc. Lett. 284, 157–167.

491 Lord, O.T., Wann, E.T.H., Hunt, S. a., Walker, A.M., Santangeli, J., Walter, M.J., Dobson,
492 D.P., Wood, I.G., Vočadlo, L., Morard, G., Mezouar, M., 2014. The NiSi melting curve
493 to 70GPa. Phys. Earth Planet. Inter. 233, 13–23. doi:10.1016/j.pepi.2014.05.005

494 McDonough, W.F., 2003. Compositional Model for the Earth's Core. Treatise in
495 Geochemistry 2, 547–568.

496 McNamara, A.K., Garnero, E.J., Rost, S., 2010. Tracking deep mantle reservoirs with ultra-
497 low velocity zones. Earth Planet. Sci. Lett. 299, 1–9. doi:10.1016/j.epsl.2010.07.042

498 Mezouar, M., Crichton, W.A., Bauchau, S., Thurel, F., Witsch, H., Torrecillas, F., Blattman,
499 G., Marion, P., Dabin, Y., Chavanne, J., Hignette, O., Morawe, C., Borel, C., 2005.
500 Development of a new state-of-the-art beamline optimized for monochromatic single
501 crystal and powder X-ray diffraction under extreme conditions at the ESRF. J. Synch.
502 Rad. 12, 659–664.

503 Morard, G., Andrault, D., Antonangeli, D., Bouchet, J., 2014. Properties of iron alloys under
504 the earth's core conditions. Comptes Rendus - Geosci. 346, 130–139.
505 doi:10.1016/j.crte.2014.04.007

506 Morard, G., Andrault, D., Guignot, N., Sanloup, C., Mezouar, M., Petitgirard, S., Fiquet, G.,
507 2008. In situ determination of {F}e-{F}e_3{S} phase diagram and liquid structural
508 properties up to 65 {GP}a. Earth Planet. Sci. Lett. 272, 620–626. doi:DOI:
509 10.1016/j.epsl.2008.05.028

510 Morard, G., Andrault, D., Guignot, N., Siebert, J., Garbarino, G., Antonangeli, D., 2011.
511 Melting of Fe-Ni-Si and Fe-Ni-S alloys at megabar pressures: implications for the Core-
512 Mantle Boundary temperature. Phys. Chem. Miner. 38, 767–776.

513 Morard, G., Siebert, J., Andrault, D., Guignot, N., Garbarino, G., Guyot, F., Antonangeli, D.,
514 2013. The Earth's core composition from high pressure density measurements of liquid
515 iron alloys. Earth Planet. Sci. Lett. 373, 169–178. doi:10.1016/j.epsl.2013.04.040

516 Mori, Y., Ozawa, H., Hirose, K., Sinmyo, R., Tateno, S., Morard, G., Ohishi, Y., 2016.
517 Melting experiments on Fe–Fe3S system to 254 GPa. Earth Planet. Sc. Lett. 464, Under
518 Review. doi:10.1016/j.epsl.2017.02.021

519 Nomura, R., Hirose, K., Uesugi, K., Ohishi, Y., Tsuchiyama, A., Miyake, A., Ueno, Y., 2014.
520 Low core-mantle boundary temperature inferred from the solidus of pyrolite. Science
521 343, 522–5. doi:10.1126/science.1248186

522 Ohta, K., Cohen, R.E., Hirose, K., Haule, K., Shimizu, K., Ohishi, Y., 2012. Experimental
523 and theoretical evidence for pressure-induced metallization in FeO with rocksalt-type
524 structure. Phys. Rev. Lett. 108, 1–5. doi:10.1103/PhysRevLett.108.026403

525 Ozawa, H., Hirose, K., Mitome, M., Bando, Y., Sata, N., Ohishi, Y., 2008. Chemical
526 equilibrium between ferropericlase and molten iron to 134 GPa and implications for iron
527 content at the bottom of the mantle. Geophys. Res. Lett. 35, 5308.

528 Ozawa, H., Hirose, K., Mitome, M., Bando, Y., Sata, N., Ohishi, Y., 2008. Chemical
529 equilibrium between ferropericlase and molten iron to 134 GPa and implications for iron
530 content at the bottom of the mantle. Geophys. Res. Lett. 35, 1–5.

531   doi:10.1029/2007GL032648

532 Ozawa, H., Hirose, K., Yonemitsu, K., Ohishi, Y., 2016. High-pressure melting experiments
533   on Fe???Si alloys and implications for silicon as a light element in the core. Earth Planet.
534   Sci. Lett. 456, 47–54. doi:10.1016/j.epsl.2016.08.042

535 Poirier, J.P., 1994. Light elements in the Earth's outer core: A critical review. Phys. Earth
536   Planet. Inter. 85, 319–337.

537 Pradhan, G.K., Fiquet, G., Siebert, J., Auzende, A.-L., Morard, G., Antonangeli, D.,
538   Garbarino, G., 2015. Melting of MORB at core–mantle boundary. Earth Planet. Sci. Lett.
539   431, 247–255. doi:10.1016/j.epsl.2015.09.034

540 Rudge, J.F., Kleine, T., Bourdon, B., 2010. Broad bounds on Earth's accretion and core
541   formation constrained by geochemical models. Nat. Geosci. 3, 439–443.

542 Sakamaki, K., Takahashi, E., Nakajima, Y., Nishihara, Y., Funakoshi, K., Suzuki, T., Fukai,
543   Y., 2009. Melting phase relation of FeHx up to 20 GPa: Implication for the temperature
544   of the Earth's core. Phys. Earth Planet. Inter. 174, 192–201.
545   doi:10.1016/j.pepi.2008.05.017

546 Seagle, C.T., Heinz, D.L., Campbell, A.J., Prakapenka, V.B., Wanless, S.T., 2008. Melting
547   and thermal expansion in the Fe-FeO system at high pressure. Earth Planet. Sci. Lett.
548   265, 655–665. doi:10.1016/j.epsl.2007.11.004

549 Siebert, J., Badro, J., Antonangeli, D., Ryerson, F., 2013. Terrestrial Accretion Under
550   Oxidising Conditions. Science (80-.). 1194. doi:10.1126/science.1227923

551 Siebert, J., Badro, J., Antonangeli, D., Ryerson, F.J., 2013. Terrestrial accretion under
552   oxidizing conditions. Science 339, 1194–7. doi:10.1126/science.1227923

553 Tateno, S., Hirose, K., Ohishi, Y., Tatsumi, Y., 2010. The structure of iron in Earth's inner
554   core. Science (80-.). 330, 359–361.

555 Torchio, R., Boccato, S., Cerantola, V., Morard, G., Irifune, T., Kantor, I., Boccato, S.,
556   Cerantola, V., Morard, G., Irifune, T., Kantor, I., 2016. Probing the local , electronic and
557   magnetic structure of matter under extreme conditions of temperature and pressure. High
558   Press. Res. 7959. doi:10.1080/08957959.2016.1198904

559 Tsuno, K., Ohtani, E., 2009. Eutectic temperatures and melting relations in the Fe-O-S system
560   at high pressures and temperatures. Phys. Chem. Miner. 36, 9–17. doi:10.1007/s00269-
561   008-0254-2

562 Wenk, H.-R., Matthies, S., Hemley, R., Mao, H.-K., Shu, J., 2000. The plastic deformation of
563   iron at pressures of the Earth's inner core. Nature 405, 1044–1047.
564   doi:10.1038/35016558

565 Williams, Q., Garnero, E.J., 1996. Seismic Evidence for Partial Melt at the Base of Earth's
566   Mantle. Science (80-.). 273, 1528–1530.

567

Tables:

Rietveld analysis	Pressure (Gpa)	Temperature (K)	wt%O	wt%C	%atO	%atC
Fe5wtO_2_27	44.10±1.53	3020±150	3.34±1	2.74±1	9.85±3.5	10.78±4.3
Fe5wtO_2_43	56.79±1.58	3110±150	2.00±1	2.27±1	6.17±3.5	9.33±4.3
Fe5wtO_4_21	40.84±1.60	3150±150	0.44±1	1.40±1	1.46±3.5	6.15±4.3
Fe5wtO_4_65	60.92±1.43	2850±150	1.11±1	0.80±1	3.68±3.5	3.53±4.3
Fe5wtO_4_94	64.98±1.85	3600±150	2.45±1	1.00±1	7.79±3.5	4.25±4.3
Fe5wtO_4_118	67.12±1.78	3480±150	1.78±1	0.96±1	5.77±3.5	4.04±4.3
Fe5wtO_7_42	81.00±1.91	3700±150	7.79±1	0.58±1	22.38±3.5	2.23±4.3
Fe5wtO_7_63	78.94±1.57	3100±150	4.45±1	1.75±1	13.23±3.5	6.92±4.3
SEM-FEG analysis	Pressure (Gpa)	Temperature (K)	wt%O		%atO	
NK27 LH2	46±5	2780±150	1.54±0.16		5.18±0.69	
NK27 LH1	36±5	2400±150	1.56±0.2		5.24±0.56	
NK30	102±5	3060±150	10.03±0.5		30.37±1.7	
FeO3	81.18±1.57	3100±150	5.73±0.5		18.81±1.7	
FeO9	74.41±1.53	2990±150	2.6±0.5		8.52±1.7	
FeO1	105.45±1.51	3030±150	10.4±0.5		28.83±1.7	
Microprobe analysis						
NK30	102±5	3060±150	10.11±1.13		27.34±3.83	
FeO3	81.18±1.57	3100±150	6.96±0.13		23.15±0.45	

Table 1 : Chemical analyses performed on Fe-O samples using different techniques (EDX

analyses using the FEG-SEM, WDS analyses using an electron microprobe and Rietveld

analysis of re-heated samples after quench). EDX measurements below 2wt% may not be

reliable, due to peak interference between Fe and O. The Rietveld analysis emphasizes the

carbon contamination of the sample after melting. This contamination has not been analysed in

the samples analysed by electron probe.

Rietveld analysis	Pressure (GPa)	Temperature (K)	wt%C	at%C
Fe1-5wtC4_90	39.94±1.57	3100±150	2.67±1	11.33±4.3
Fe1-5wtC4_148	51.25±1.4	2800±150	3.93±1	16±4.3
Fe1-5wtC4_223	78.12±1.88	3650±150	3.40±1	14.09±4.3
Fe1-5wtC4_243	74.94±1.45	3600±150	3.96±1	16.08±4.3
Fe1-5wtC7_13	28.77±1.23	2500±150	3.34±1	13.86±4.3

Fe1-5wtC7_29	35.82±1.4	2800±150	2.93±1	12.33±4.3
Fe1-5wtC7_49	43.73±1.63	3200±150	2.57±1	10.94±4.3
Fe1-5wtC7_76	52.07±1.57	3100±150	2.88±1	12.14±4.3
Fe1-5wtC7_101	58.92±1.6	3160±150	2.54±1	10.82±4.3
Fe4wtC5_47	31.48±1.57	3100±150	3.71±1	15.22±4.3
Fe4wtC5_70	34.15±2.08	4000±150	4.23±1	17.05±4.3
Fe4wtC5_89	41.19±1.42	2830±150	3.01±1	12.63±4.3
HC2481-Fe1-5wtC1_42	81.53±1.59	3130±150	3.18±1	13.25±4.3
HC2481-Fe1-5wtC2_27	107.85±1.42	2840±150	3.57±1	14.70±4.3

597

598 **Table 2 :** Rietveld analysis of re-heated samples in the Fe-Fe$_3$C system. The assumption of zero

599 C solubility in pure Fe may have led to a small underestimate of C content in the liquid. In

600 support of our approximation we stress that this solubility has been documented to be lower

601 than 0.7 wt%C at 20 GPa (Fei and Brosh, 2014), and to decrease with pressure (O T Lord et al.,

602 2009). Furthermore, as the sample is kept under moderate temperature (~1500 K), solubility of

603 C in solid Fe should be even lower.

604

	a	c	P_0 (GPa)	T_0 (K)
Fe-S	10.5	3	21	1260
Fe-O	17	3.8	0	1800
Fe-C	8.5	3.8	0	1420
Fe-18at%Si	23.6	1.89	0	1600

605

606 **Table 3**: **Fit parameters of the Simon–Glatzel equation $T_{melt} = T_0 [(P_{melt}-P_0)/a +1]^{1/c}$.** In

607 the case of Fe-18 at.% Si the fit parameters are from (Fischer et al., 2013)

608

609

Light element	Teut at CMB (K)	Eut content (at %)	Slope (K/at%)
S	2870 (± 200)	15 (± 5)	89 (±56)
Si	-	4	-
O	3200 (± 200)	30 (± 3)	33 (±11)

| | C | 2990 (± 200) | 11 (± 5) | 110 (±80) |

611 **Table 4**: **Eutectic temperature and composition at the CMB pressure for selected Fe-X**

612 **binary systems.** A linear interpolation between pure Fe and the eutectic composition for each

613 system is used to estimate the melting depression induced by each light element. The melting

614 point of pure Fe at 136 GPa is taken as 4200 K (Anzellini et al., 2013). Eutectic temperatures

615 for the Fe-Si system (4 at%Si (Ozawa et al., 2016)) have not been measured, but the difference

616 with respect to pure Fe can be considered negligible. See text for details.

617

Figure legends

Figure 1: **Electron back scattering image of an Fe-FeO sample recovered after laser**

heating at 41 GPa. The sample is embedded in a KCl pressure medium. Two different sample

regions were heated to temperatures just above (LH1) and just below (LH2) the melting point.

Identification of the hotspot has been performed by correlating SEM and transmitted light

images. Significant changes in microstructure are observed only for LH1. We also report the

X-ray diffraction patterns collected during laser heating at each sample location, emphasizing

the appearance of a diffuse scattering signal at LH1 and its absence at LH2.

Figure 2: Rietveld analysis of an integrated XRD spectrum of a quenched and

recrystallized liquid at 41.2±1.4 GPa and 2830±150 K. The corresponding diffraction image

is shown at the top right of the figure. All diffraction peaks (plus symbols) could be indexed to

Fe, Fe_3C or KCl (tick marks). Peak intensity was closely reproduced using Rietveld analysis

performed with the GSAS software (red line) leaving a minimal residual (blue line). The

intensity ratio of the three diffraction lines of hcp Fe is close to ideal suggesting hydrostatic

conditions prevail and there is minimal preferred orientation (Wenk et al., 2000).

Figure 3: **Eutectic melting curves for Fe-Fe_3C and Fe-FeO systems**. Solid symbols represent

the last temperature at which the X-ray diffraction pattern showed no sign of liquid diffuse

scattering; open symbols correspond to the first appearance of diffuse scattering (see Tables S1,

S2 and S3). Our data are in remarkable agreement with previous experimental reports (Lord et

al. 2009; Seagle et al. 2008). Hexagons represent the melting of pure Fe based on XANES

measurements as reported by (Aquilanti et al., 2015). Solid red lines represent fits to midpoints

between the closest open and solid symbols, using the Simon–Glatzel equation (fitting

643   parameters are reported in Table 3). All data fall within a constant error envelope of ±200K,

644   symbolised as a shaded area around the fitted curve.

645

646   **Figure 4: Evolution of the eutectic composition with pressure in the Fe-FeO system.** The

647   eutectic composition shows a drastic increase after 50 GPa, corresponding to the metal-insulator

648   transition in the FeO end-member (Ohta et al., 2012). This evolution is different from previous

649   experimental (Seagle et al., 2008) and thermodynamic (Komabayashi, 2014) studies but leads

650   to a comparable value for the O content in the eutectic liquid (11 wt%O or 30 at%O) at the

651   CMB pressure of 136 GPa (Table 1).

652

653   **Figure 5: Evolution of the eutectic composition with pressure in the Fe-Fe$_3$C system.** Open

654   squares are Rietveld analyses of quenched samples and assume no carbon solubility in the solid

655   iron phase. Our results are in good agreement with experimental values measured in large

656   volume press experiments (Fei and Brosh, 2014) but differ from their thermodynamic

657   modelling at high pressure. Our best estimate for C content in the eutectic liquid at the CMB is

658   2.6 wt%C (11 at%C).

659

660   **Figure 6: Eutectic melting curve of iron alloys (solid lines) compared to solidus curves of**

661   **mantle lithologies (dashed lines) as a function of pressure.** Melting curves for the Fe-alloys

662   were recalculated using the Simon-Glatzel equation and the parameters reported in Table 3.

663   Melting temperatures at the CMB for mantle lithologies are as follows: chondritic (Andrault et

664   al., 2011) and peridotitic (Fiquet et al., 2010) mantle ~4100-4200 K, MORB ~3750-4000 K

665   (Andrault et al., 2014; Pradhan et al., 2015), and hydrated pyrolite ~3600 K (Nomura et al.,

666   2014).

667

668 **Figure 7**: **A) Liquidus temperatures in Fe-X systems compared with melting temperatures**

669 **of mantle materials at the CMB (136 GPa).** Thick solid lines are linear interpolations between

670 the melting point of pure Fe (open circle) (Anzellini et al., 2013) and the eutectic compositions

671 determined here or in previous works (Table 4). Solidi at CMB pressure for peridotitic (Fiquet

672 et al., 2010) and MORB mantle (Andrault et al., 2014; Pradhan et al., 2015) are represented by

673 horizontal bands. **B) Expected temperature at the CMB for a core with a binary Fe-X**

674 **composition.** Temperature is estimated by shifting the crystallisation temperature of the Fe-X

675 alloy by ΔT_{CMB}=400-900 K. To account for this temperature difference between the adiabat

676 and the crystallisation temperature of the iron alloys, the light element content in the Earth's

677 outer core could be estimated.

678

	P (GPa)	dP (GPa)	T (K)	dT (K)	a KCl (Å)	
Fe_1-5wtC_4_47	24.32	0.97	2030	150	3.3107	SOL
Fe_1-5wtC_4_49	23.91	1.06	2180	150	3.3174	LIQ
Fe_1-5wtC_4_86	38.34	1.04	2150	150	3.1994	SOL
Fe_1-5wtC_4_88	39.21	1.33	2670	150	3.1994	LIQ
Fe_1-5wtC_4_144	50.35	1.13	2310	150	3.1309	SOL
Fe_1-5wtC_4_145	50.71	1.22	2480	150	3.1305	LIQ
Fe_1-5wtC_4_171	60.97	1.28	2580	150	3.0827	SOL
Fe_1-5wtC_4_173	61.31	1.39	2780	150	3.0827	LIQ
Fe_1-5wtC_4_236	73.48	1.31	2630	150	3.0332	SOL
Fe_1-5wtC_4_239	74.26	1.62	3190	150	3.0338	LIQ
Fe_1-5wtC_6_19	146.54	1.54	3050	150	2.8459	SOL
Fe_1-5wtC_6_21	147.79	1.96	3790	150	2.8459	LIQ
Fe_1-5wtC_6_44	148.90	1.50	2970	150	2.8412	SOL
Fe_1-5wtC_6_45	149.04	1.54	3050	150	2.8412	LIQ
Fe_1-5wtC_7_24	34.96	0.95	2000	150	3.2209	SOL
Fe_1-5wtC_7_26	35.47	1.15	2350	150	3.2215	LIQ
Fe_1-5wtC_7_46	42.11	1.04	2160	150	3.1756	SOL
Fe_1-5wtC_7_48	43.06	1.40	2800	150	3.1764	LIQ
Fe_1-5wtC_7_70	51.46	1.13	2310	150	3.1252	SOL
Fe_1-5wtC_7_71	51.62	1.18	2400	150	3.1252	LIQ
Fe_1-5wtC_7_114	58.80	1.26	2550	150	3.0921	SOL
Fe_1-5wtC_7_115	58.89	1.29	2600	150	3.0921	LIQ
HC2481_Fe1-5wtC1_16	71.06	1.20	2440	150	3.0410	SOL
HC2481_Fe1-5wtC1_17	71.01	1.27	2570	150	3.0420	LIQ
HC2481_Fe1-5wtC1_37	82.35	1.26	2540	150	3.0020	SOL
HC2481_Fe1-5wtC1_39	82.09	1.27	2570	150	3.0030	LIQ
HC2481_Fe1-5wtC2_25	108.73	1.32	2660	150	2.9270	SOL

HC2481_Fe1-5wtC2_27	107.85	1.43	2840	150	2.9300	LIQ

Table S1 : Melting temperatures for Fe-1.5wt%C samples. The last solid and the first liquid temperatures allowed us to bracket the eutectic melting curve. The cell parameter of the KCl pressure medium is indicated, as it has been used to determine the thermal pressure.

	P (GPa)	dP (Gpa)	T (K)	dT (K)	a KCl	
Fe10O3_13	43.97	1.15	2340	150	3.1663	SOL
Fe10O3_14	44.14	1.25	2520	150	3.1671	LIQ
Fe10O3_31	63.25	1.22	2470	150	3.0722	SOL
Fe10O3_34	63.61	1.32	2660	150	3.072	LIQ
Fe10O6_60	92.52	1.54	3050	150	2.973	SOL
Fe10O6_62	93.71	1.97	3820	150	2.9733	LIQ
Fe10O7_12	88.23	1.45	2880	150	2.9851	SOL
Fe10O7_14	89.74	1.57	3100	150	2.9816	LIQ
Fe10O7_30	97.49	1.39	2780	150	2.9574	SOL
Fe10O7_32	98.80	1.63	3200	150	2.9557	LIQ
Fe10O9_30	95.94	1.56	3080	150	2.9632	SOL
Fe10O9_31	96.70	1.77	3450	150	2.9628	LIQ
Fe10O11_23	73.63	1.29	2590	150	3.0324	SOL
Fe10O11_24	74.16	1.38	2760	150	3.0315	LIQ
Fe10O11_51	86.26	1.51	3000	150	2.9919	SOL
Fe10O11_53	86.21	1.59	3140	150	2.9928	LIQ
Fe10O12_33	116.99	1.57	3090	150	2.9086	SOL
Fe10O12_36	119.41	1.96	3800	150	2.9057	LIQ

Table S2 : Melting temperature for Fe-10wt%O samples. The last solid and the first liquid temperatures allowed us to bracket the eutectic melting curve. The cell parameter of the KCl pressure medium is indicated, as it has been used to determine the thermal pressure.

	P (GPa)	dP (Gpa)	T (K)	dT (K)	a KCl (Å)	
Fe5wtO1_25	80.04	1.49	2950	150	3.012	sol
Fe5wtO1_28	84.57	1.99	3850	150	3.0019	liq
Fe5wtO1_41	93.67	1.45	2880	150	2.9688	sol
Fe5wtO1_44	94.99	1.64	3220	150	2.9666	liq
Fe5wtO1_63	105.39	1.64	3220	150	2.938	sol
Fe5wtO1_65	105.55	1.91	3700	150	2.9397	liq
Fe5wtO2_20	44.53	1.26	2540	150	3.165	sol
Fe5wtO2_22	44.76	1.38	2760	150	3.1658	liq
Fe5wtO2_38	56.37	1.29	2590	150	3.1036	sol
Fe5wtO2_39	56.37	1.34	2680	150	3.1043	liq
Fe5wtO4_17	40.44	1.17	2390	150	3.1884	sol
Fe5wtO4_18	40.60	1.26	2540	150	3.189	liq
Fe5wtO4_38	53.59	1.23	2490	150	3.1161	sol
Fe5wtO4_39	53.86	1.32	2650	150	3.1161	liq
Fe5wtO4_61	60.55	1.34	2680	150	3.0853	sol
Fe5wtO4_62	60.92	1.43	2850	150	3.0849	liq
Fe5wtO4_88	63.53	1.30	2610	150	3.072	sol
Fe5wtO4_89	63.63	1.35	2700	150	3.0722	liq
Fe5wtO4_113	65.64	1.36	2730	150	3.0641	sol
Fe5wtO4_114	65.80	1.43	2840	150	3.0642	liq
Fe5wtO7_56	77.82	1.51	3000	150	3.0199	sol
Fe5wtO7_58	78.21	1.62	3180	150	3.0196	liq
Fe5wtO8_11	32.40	1.15	2350	150	3.2444	sol
Fe5wtO8_13	33.03	1.18	2400	150	3.2402	liq
HC2481_Fe5wtO_1_23	103.04	1.49	2950	150	2.943	sol
HC2481_Fe5wtO_1_24	103.09	1.50	2980	150	2.943	liq
HC2481_Fe5wtO_2_22	57.07	1.19	2420	150	3.099	sol
HC2481_Fe5wtO_3_29	79.80	1.41	2810	150	3.012	sol

HC2481_Fe5wtO_3_31	80.28	1.47	2920	150	3.011	liq
HC2481_Fe5wtO_7_32	149.41	1.63	3210	150	2.841	sol
HC2481_Fe5wtO_7_35	148.10	1.73	3380	150	2.844	liq
HC2481_Fe5wtO_8_24	42.13	1.13	2310	150	3.177	sol
HC2481_Fe5wtO_8_25	42.55	1.16	2360	150	3.175	liq
HC2481_Fe5wtO_9_39	74.75	1.35	2700	150	3.029	sol
HC2481_Fe5wtO_9_44	74.41	1.51	2990	150	3.032	liq
HC2481_Fe5wtO_9_61	86.42	1.37	2740	150	2.99	sol
HC2481_Fe5wtO_9_62	87.00	1.45	2890	150	2.989	liq

Table S3 : Melting temperature for Fe-5wt%O samples. The last solid and the first liquid temperatures allowed us to bracket the eutectic melting curve. The cell parameter of the KCl pressure medium is indicated, as it has been used to determine the thermal pressure.
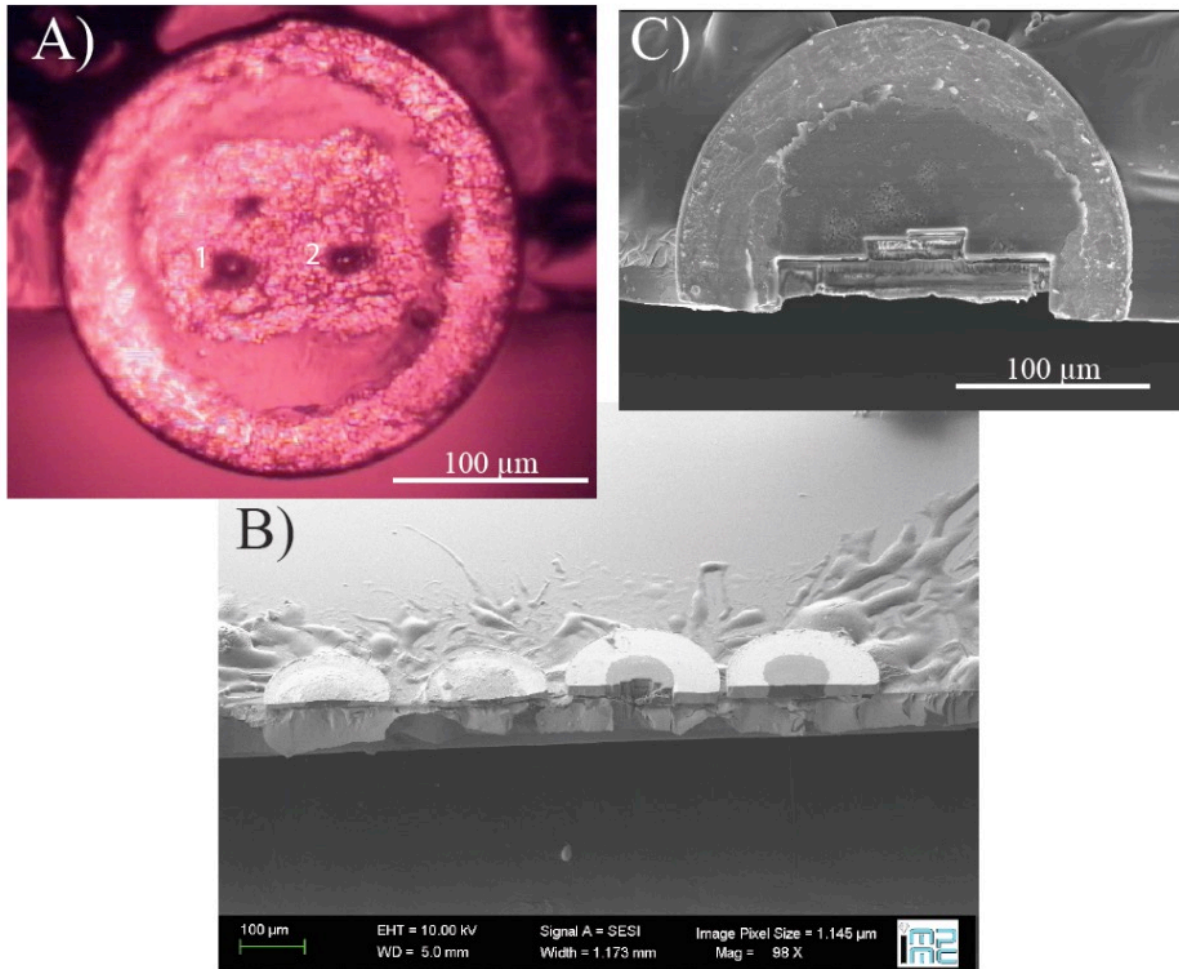
Supplementary Figures

Figure S1: **Optical and backscattered electron images describing the procedure for the analysis of recovered samples.** A) Sample chamber after laser cutting placed on a glass slide. Two laser-heated spots can be clearly identified (1 and 2). B) SEM image of four different samples after ion polishing. C) SEM image of a sample after FIB cutting.
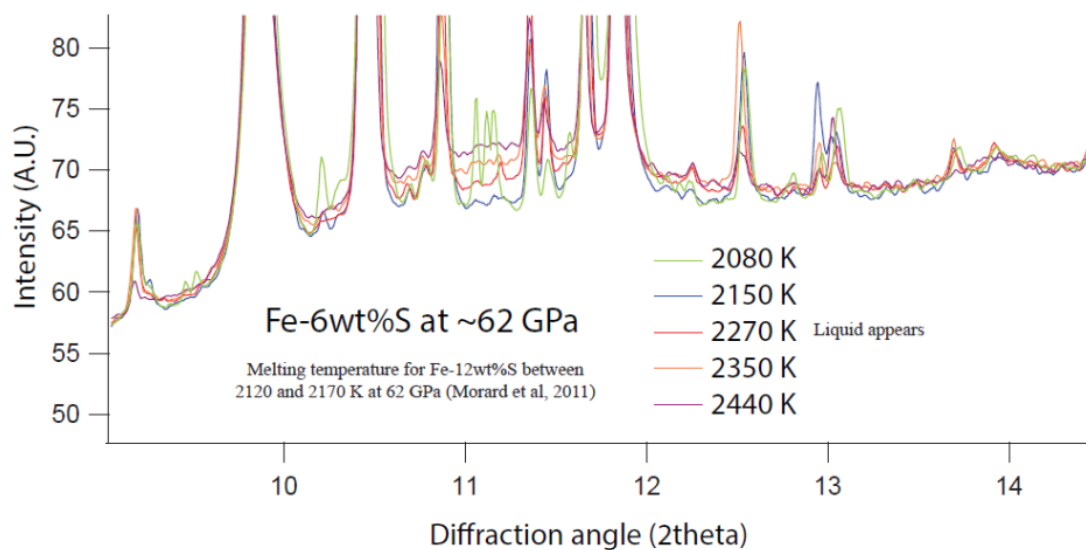
Figure S2: Integrated XRD spectra collected on an Fe-S sample with 6 wt.% S at 62 GPa and increasing temperature. Melting occurs between 2150 K and 2270 K at ~62 GPa. This temperature is in very good agreement with previous measurements performed on a sample with an initial composition of 12 wt.% S, where melting was bracketed between 2120 K and 2170 K (Morard et al., 2011). We note that the eutectic composition at this pressure has been measured as ~10 wt.% S (Kamada et al., 2012; Morard et al., 2008).

References

Kamada, S., Ohtani, E., Terasaki, H., Sakai, T., Miyahara, M., Ohishi, Y., Hirao, N., 2012. Melting relationships in the Fe–Fe3S system up to the outer core conditions. Earth Planet. Sc. Lett. 359–360, 26–33.

Morard, G., Andrault, D., Guignot, N., Sanloup, C., Mezouar, M., Petitgirard, S., Fiquet, G., 2008. In situ determination of {F}e-{F}e_3{S} phase diagram and liquid structural properties up to 65 {GP}a. Earth Planet. Sci. Lett. 272, 620–626. doi:DOI: 10.1016/j.epsl.2008.05.028

Morard, G., Andrault, D., Guignot, N., Siebert, J., Garbarino, G., Antonangeli, D., 2011.
Melting of Fe-Ni-Si and Fe-Ni-S alloys at megabar pressures: implications for the Core-
Mantle Boundary temperature. Phys. Chem. Miner. 38, 767–776.